JGR Solid Earth

RESEARCH ARTICLE
10.1029/2019JB019206

Key Points:
- Magnetotelluric data collected in central and south Tibetan Plateau highlight distinct variations in the crustal conductivity structure
- Empirical relationship between conductivity and viscosity helps identifying stark rheological contrast in the lower crust
- Rheological contrast can lead to divergent mechanical deformations, which further shape the complex surface structure of the Plateau

Supporting Information:
- Supporting Information S1

Correspondence to:
H. Dong,
donghao@cugb.edu.cn

Citation:
Dong, H., Wei, W., Jin, S., Ye, G., Jones, A. G., Zhang, L., et al. (2020). Shaping the surface deformation of central and south Tibetan Plateau: Insights from magnetotelluric array data. *Journal of Geophysical Research: Solid Earth*, *125*, e2019JB019206. https://doi.org/10.1029/2019JB019206

Received 6 DEC 2019
Accepted 1 JUL 2020
Accepted article online 2 JUL 2020

Shaping the Surface Deformation of Central and South Tibetan Plateau: Insights From Magnetotelluric Array Data

Hao Dong[1,2], Wenbo Wei[1,2], Sheng Jin[1,2], Gaofeng Ye[1,2], Alan G. Jones[1,3,4], Letian Zhang[1,2], Jian'en Jing[1,2], Chengliang Xie[1,2], and Yaotian Yin[1,2]

[1]School of Geophysics and Information Technology, China University of Geosciences, Beijing, China, [2]State Key Laboratory of Geological Processes and Mineral Resources, China University of Geosciences, Beijing, China, [3]Dublin Institute for Advanced Studies, Dublin, Ireland, [4]Complete MT Solutions Inc., Ottawa, Canada

Abstract The ongoing India-Asia collision since the Paleogene created the Tibetan Plateau, the most prominent elevated plateau on our planet. This convergence also contributed to the formation of two distinct types of active surface deformation of the plateau, namely, north–south trending normal fault systems and "conjugate" strike-slip fault systems. The tectonics and geodynamic mechanism(s) behind this curious combination are still unclear, despite numerous theories proposed over past decades. Here we present a new three-dimensional, lithospheric-scale, electrical conductivity model with unprecedented resolution of the central part of Tibetan Plateau derived from the SINOPROBE magnetotelluric array data set and discuss its inferences related to this question. Our model reveals contrasting conductivity structures corresponding to the surface deformation patterns, namely, highly conductive lower crustal anomalies beneath the graben systems in the Lhasa and Qiangtang terranes and moderately resistive crustal features in the strike-slip region near Bangong-Nujiang Suture Zone. With the help of experimentally calibrated constraints between conductivity and melt fraction, the conductivity model and the inferred lateral viscosity distribution together suggest a weak lower crust beneath the graben regions, compared to a stronger crustal rheology associated with the strike-slip zone. Here we expand the previously proposed "extensional extrusion" tectonic model in central Tibet to interpret our conductivity model and other geophysical/geodesic observations. The weak rheology under a N-S directed primary stress may have caused the east–west extension of the graben regions, which further aides the eastward extrusion of the conjugate strike-slip zone and eventually shapes the surface deformation of central Tibetan Plateau into its current, complex pattern.

Plain Language Summary The collision between the Indian and Asian continents built the Tibetan Plateau, the highest plateau in the world. This active collision also formed distinctly different types of large-scale geological structures on the plateau surface. Among the most important features on the plateau, the origin of the N-S directed normal (or spreading) fault zones in two regions named Lhasa and Qiangtang, and the NW/SE directed slip fault zones between these two regions are still unclear. In order to understand the generation of those structures, we use a geophysical imaging method called magnetotellurics to measure the naturally occurring electromagnetic waves in the earth. We model and analyze these magnetotellurics data to obtain the deep structure beneath those surface structures, using sophisticated computer codes. We find that the two dominant but different types of those structures are most likely due to the different strengths of the deep crust. This strength difference can lead to a mechanical stress contrast, which further builds the distinctly different surface structures. These kinds of deep physical structure differences have not been detected for the area before. Our study provides information on the strength of the crust, which is critical to understand the deep mechanic process of the earth.

1. Introduction

Aside from its great average elevation of ~4,500 m, the surface of the Tibetan Plateau is characterized by a combination of synchronous normal and strike-slip faulting (Taylor & Yin, 2009) accommodating the convergence of India and Asia. Along with the fast surface motion revealed by geodesic measurements (Gan

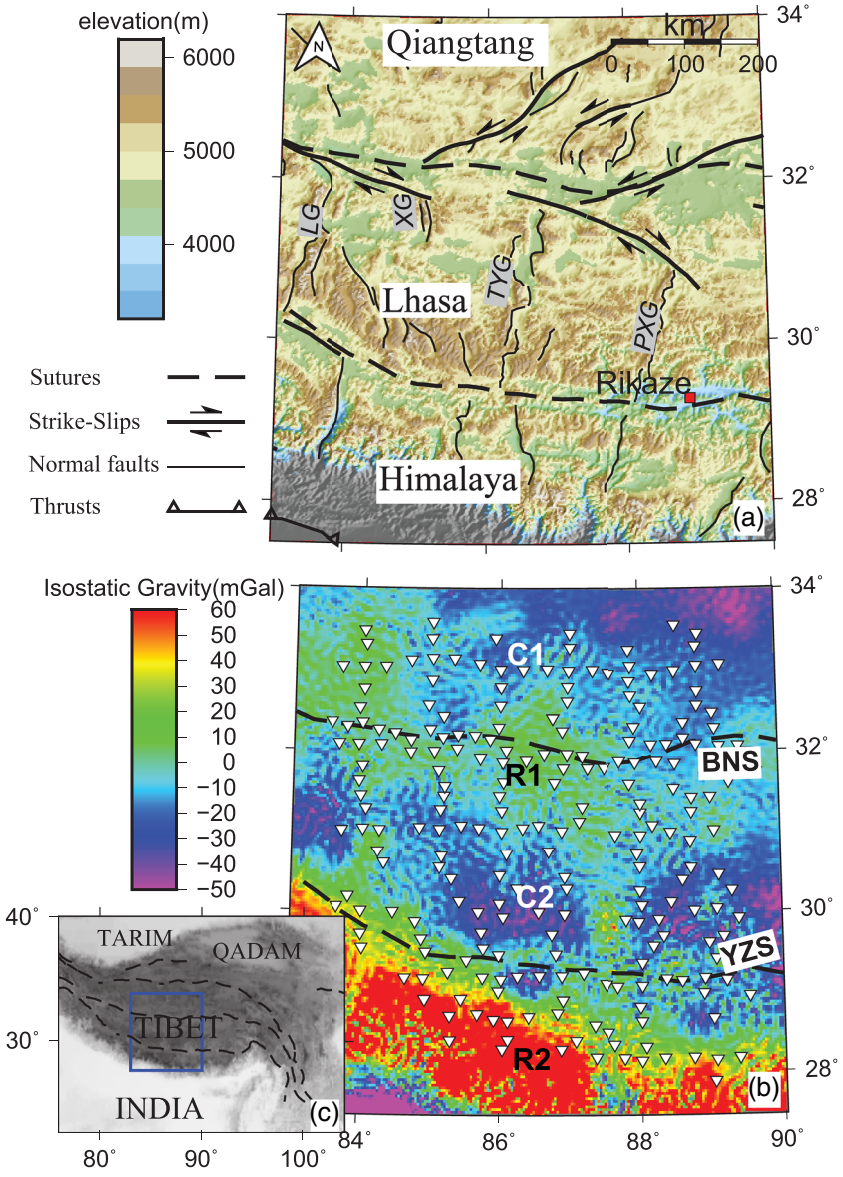

Figure 1. (a) Topography relief map of central Tibet with major tectonic features indicated. (b) Airy–Heiskanen Isostasy gravity anomaly map superimposed by the Magnetotelluric array layout for the stations used in this study. (c) Relative position of the area of MT survey (blue box) in Tibetan Plateau. BNS: Bangong-Nujiang Suture zone; YZS: Yarlung-Zangbo Suture zone; MBT: Main Boundary Thrust; LG: Lunggar Graben; XG: Xiakangjian Graben; TYG: Tangra-Yum Co Graben; PXG: Pumqu-Xianza Graben; Lhasa: Lhasa terrane; Himalaya: Himalaya terrane; Qiangtang: Qiangtang terrane; the red square in (a) indicates the location of the city of Rikaze; the labels C1, C2, R1, and R2 indicate the locations of resistivity anomalies in Figure 3; gravity data are from WGM2012, downloaded from http://bgi.omp.obs-mip.fr/data-products/Grids-and-models/wgm2012 website.

et al., 2007), these active structures indicate that Tibet is still being affected by ongoing geodynamic processes associated with the collisional orogeny. Extensive geological, geodetical, and geophysical studies have been carried out for decades to try to understand the curious pattern of the distribution of these surface deformations, namely, (1) the nearly north–south trending graben zones formed by normal faults in south Lhasa and Qiangtang terranes and (2) the V-shaped "conjugate" strike-slip zone near the Bangong-Nujiang Suture (BNS) zone (Figure 1a). The graben zones consist of a series of active grabens or rifts, dating from 15 to 5 Ma, with a remarkably similar E-W spacing of order 200–300 km (e.g., Kapp et al., 2008). Located between these graben zones, the strike-slip zone features right-facing (or "<" shape) NE/SE conjugate strike-slip faults (e.g., Yin & Taylor, 2011), with relative low relief topography compared to the graben zones.

Many independent and competing models have been proposed to explain the normal and strike-slip systems in Tibetan plateau; a detailed overview can be found in Styron et al. (2011). Notable end-members of the diversity of models include Lateral Extrusion (Tapponnier et al., 1982) and Oroclinal Bending (D. Li & Yin, 2008) for the role of strike-slip structures and Radical Spreading (Copley, 2012) and Viscous Buckling (Bischoff & Flesch, 2018) to explain the normal fault systems. With all of these models being mechanically plausible, much of the evidence from these studies contradicts one another (Styron et al., 2011), and very few studies simultaneously consider the generation of coexisting grabens and strike-slip faults together. However, even the models that do discuss both types of the deformation, like Oblique Convergence (McCaffrey & Nabelek, 1998) and Paired General-Shear (Yin & Taylor, 2011), do not take into account the deep rheological structure of doubly thickened Tibetan Plateau crust.

The Tibetan Plateau should no longer be envisaged as either a combination of brittle blocks separated by faults (Tapponnier et al., 1982) or as a rheologically homogeneous structure spreading out under gravitation (Copley, 2012). Recent geodynamical modeling studies have revealed that the deep rheology of the crust could have been the key parameter to shape the surface deformation of the Earth (e.g., L. Liu & Hasterok, 2016). Three-dimensional (3-D) physics-based constraints offered by rheological considerations is hence needed to understand the concise mechanism(s) behind these complex combinations of distinct structures. Electrical conductivity (the inverse of electrical resistivity) has long been used to constrain crustal rheological structure (e.g., Tozer, 1981), as it is sensitive to the presence of interconnected partial melts or aqueous fluids, which also greatly impacts rock viscosity (e.g., Hashim et al., 2013; Laumonier et al., 2017; Pommier et al., 2013). With recordings of the time-varying fluctuations of the natural electromagnetic (EM) fields of the Earth, the magnetotelluric (MT) method can determine the underground conductivity distribution (e.g., Chave & Jones, 2012). Thus, MT has been be widely used to help constrain the lithospheric rheological structure and discriminate between possible/plausible geodynamic models; examples for the Tibetan Plateau include Nelson et al. (1996), S. Li et al. (2003), Bai et al. (2010), Rippe and Unsworth (2010), and Le Pape et al. (2015).

In our study, we used data from a relatively densely spaced (15–25 km, given the inhospitable terrane and our focus on the lithosphere) array of broadband (BBMT) and long period (LMT) MT sites to derive a three-dimensional resistivity model for the central and southern part of the Tibetan Plateau (28° to 34°N). Our data coverage enables development of an electrical resistivity model of unprecedented resolution for the lithosphere of the central and south part of the Plateau that allows us to resolve and define crustal and upper mantle structures beneath the region with pronounced normal and strike-slip surface deformations. From the resistivity model, we investigate the inferred likely melt generation with an experiment-calibrated relationship between electrical conductivity and melt fraction. We further constrain the lower crustal viscosity structure with the conductivity model. Finally, we propose an expanded mechanism of Extensional Extrusion to explain the conductivity and rheology structure that further reconciles the complex stress state, surface motion, and deformation pattern in central Tibetan Plateau.

2. Magnetotelluric Data and Analyses

2.1. Magnetotelluric Data

The magnetotelluric data we analyze herein were acquired from 2011 to 2013 by the China University of Geosciences, Beijing (CUGB) and are a subset of the Chinese Magnetotelluric Standard-Grid Network acquired under the SINOPROBE project (S. Dong et al., 2013)—see supporting information for a description of this network. These MT stations were synchronously recorded to remove incoherent noise using remote referencing (Gamble et al., 1979). The time-varying orthogonal electric and magnetic fields were sampled using Phoenix MTU-5 broad band MT (BBMT) and LVIV Lemi-417 long period MT (LMT) systems. Magnetic fields were measured with induction coils (BBMT) and three-component fluxgates (LMT), whereas electric channels were recorded using ~100 m long electric dipoles with nonpolarizing Pb-$PbCl_2$ electrodes. Typical recording time was 24 hr for BBMT and 7 days for LMT. The time series were analyzed and processed using robust statistic methods (LMT: Egbert & Booker, 1986; BBMT: Jones & Jödicke, 1984) to estimate MT and geomagnetic transfer functions (or tipper) for the period range of 0.1–10,000 s. The quality of the acquired MT data was generally good, and the data were mostly free of cultural electromagnetic noise, primarily because most of the central Tibetan Plateau is uninhabited and not industrialized. The extremely

rough topography in the region, on the other hand, proved to be challenging for station deployment, which contributed to the slightly irregular site distribution (Figure 1).

To date, only one other 3-D study based on the Tibetan part of SINOPROBE MT array data has been published (H. Dong et al., 2016), and this prior study discussed the geo-electrical structure of East Himalayan Syntax in the eastern part of the plateau. Our present study is mainly focused on the central part of the Tibetan Plateau, extending coverage of previous isolated two-dimensional (2-D) survey profiles into a 3-D array covering the northern Himalaya, Lhasa, and southern Qiangtang Terrane. Combining the SINOPROBE data set and previous profile data sets from INDEPTH lines 100, 500, 800, and CUGB line 3,000 (Solon et al., 2005; Unsworth et al., 2005; Wei et al., 2001; Xie et al., 2017), data from 231 MT stations were selected and analyzed in this study. The data set is comprised of 199 BBMT-only and 32 combined BBMT-LMT stations. The details of the data set can be found in the supporting information.

It should be noted that the previous INDEPTH and CUGB profiles were mostly aligned along the graben systems (which are logistically more accessible). This could pose a statistical "static shift" (Jones, 1988) downward bias of the measured resistivity, as the grabens generally contain young and conductive sediments. Our new data set not only provides coverage over three of the major graben systems (Lunggar, Tangra-Yum Co and Pumqu-Xianza systems) but also offers good control over the strike-slip region, as well as the higher elevation region between the grabens (Figure 1). The new SINOPROBE data set also provides a better constrain on the deep structures by introducing greater coverage with LMT stations. With a better distributed site layout, our combined data set provides a far superior spatial and depth sampling of the 3-D geo-electrical structure of the central Tibet. We also find that our 3-D array is less prone to the statistical static shift bias discussed above, than in prior 2-D studies along valleys.

2.2. Dimensional Analysis

The inversion and interpretation of magnetotelluric data is greatly simplified if a 2-D assumption can be justified. However, as is well known in the MT method, applying 2-D methods to data from a 3-D earth can lead to seriously misinterpreted subsurface structures (e.g., Ledo, 2005). To test the geo-electrical dimensionality of the study region, phase tensor (Caldwell et al., 2004) and induction vector (Gregori & Lanzerotti, 1980) analyses were carried out for the magnetotelluric and geomagnetic transfer functions (Figure 2). With the skin depth effect of the propagation of electromagnetic waves, signals with longer periods have deeper penetration in the earth than shorter periods (e.g., Chave & Jones, 2012). Hence, transfer function analyses at different periods can be used as an approximate indicator of electrical structure at different depths.

We use the phase tensor (PT) method as the PT parameters are, for perfect data, not affected by frequency-independent electric field galvanic distortion from shallow heterogeneities (Caldwell et al., 2004) and it is visually informative. We recognize that the PT method does have limitations in the presence of noise and/or distortion and that it is not performed within a statistical framework (Jones, 2012), but it is useful to give first-order impressions. The orientation of the PT ellipses indicates the PT strike direction, which suggests lateral conductivity variations of the underground structures. Circular ellipses, on the other hand, indicate one-dimensional (1-D) structure (i.e., no major lateral variations). The PT skew angle β is represented by the color fills of the ellipses and displays the asymmetry in MT responses due to 3-D dimensionality. Note that $\varphi = 2 \times \beta$ is used here for a better demonstration of dimensionality. Generally, $\beta < 3°$ (or $\varphi < 6°$) is required for the data to satisfy 1-D or 2-D assumptions (Booker, 2014), which means anything other than light green color suggests 3-D structures in Figure 2, or high scatter symptomatic of large bias or statistical errors (Jones, 2012).

Geomagnetic transfer functions, which measure the ratio of the vertical component to the horizontal components of the Earth's magnetic fields, are also insensitive to electric field galvanic distortion effects caused by near-surface structures. In particular, the real part of the induction vector (in reversed Parkinson convention, Parkinson, 1959, 1962) is illustrated as arrows that point toward the direction of increasing conductance (Gregori & Lanzerotti, 1980). Consistent directions of the arrows indicate a gradient of the conductivity along the arrows.

As illustrated in Figure 2, initial PT analysis at short period (1 s) shows generally 1-D or 2-D dimensionality (light green in color and near-circular ellipses for 1-D) near the BNS but indicates moderate 3-D dimensionality (darker colors) without any consistent strike directions in the Lhasa and Qiangtang terranes. This

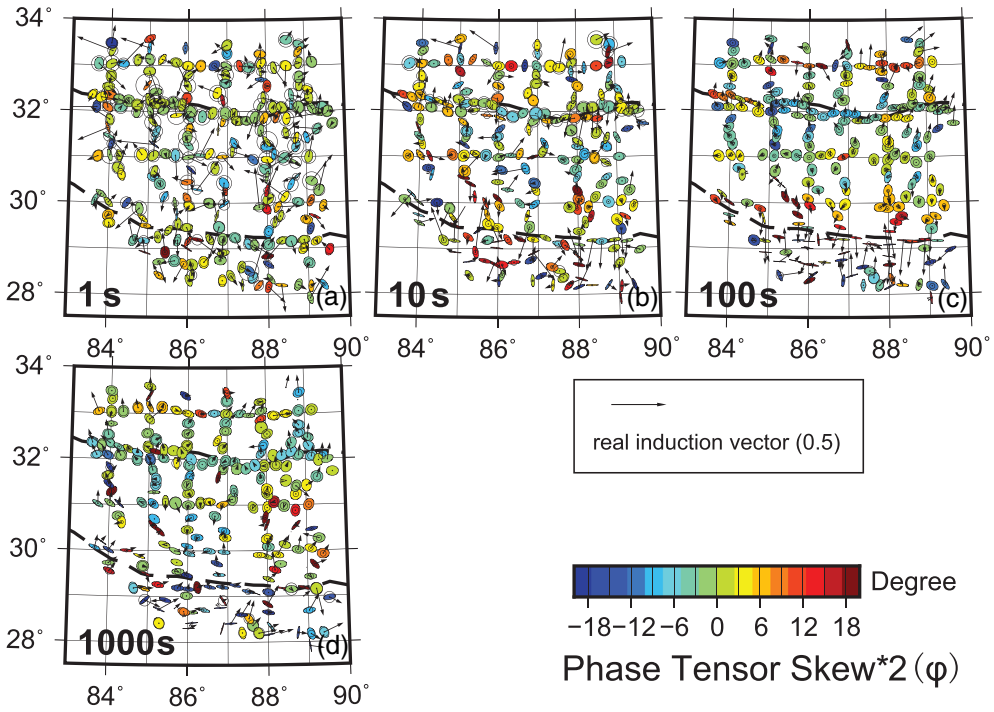

Figure 2. Maps of real geomagnetic induction vector (black arrows, reversed in Parkinson convention to point toward conductors) and magnetotelluric phase tensor (colored ellipses) at periods of 1 to 1,000 s. Note that exceedingly large induction vectors (>0.5), due to errors, are removed from the plot for a better representation. See text for detailed information.

correlates well with the random direction observed for induction arrows, which are probably pointing toward isolated shallow conductive anomalies (i.e., shallow sediments and widespread salt lakes in the central plateau). As period increases, consistent phase tensor ellipse patterns can be found near the BNS and YZS. While the ellipses all start to align in the E-W direction, they become extremely flattened with dark colors to the south (Figure 2c). This suggests strong 3-D structure and abrupt lateral geoelectrical interfaces in the E-W or N-S direction. This pattern is also consistent with the overall N-S alignment of the induction arrows. Interestingly, the boundary of the contrasting pattern seems to move north as period increases, suggesting a change of a conductivity boundary contact position with depth (Figures 2b–2d). At longer periods, the less flattened ellipses with lighter colors and the smaller magnitude of induction arrows both suggest the conductivity structures becoming less heterogeneous in the deeper parts of the study region (Figure 2d).

3. The 3-D Inversion of the MT Data

3.1. Details of the Inversion and Preferred Model

As suggested by the above dimensionality analyses, our data indicate overall 3-D structures in the study region, which of necessity calls for 3-D modeling/interpretation methods. Here the 3-D MT inversion scheme ModEM (Kelbert et al., 2014) was employed for inversion of the data. A new divergence-free system of equations was implemented that greatly improves the efficiency of the forward and adjoint calculations used in inversions (Dong & Egbert, 2019). MT and geomagnetic transfer functions at 25 equispaced periods in log domain from 0.1 to 10,000 s were inverted in this study. Error floors were set to 5% of the sqrt($|Zxy|^2$) for *Zxx* and *Zxy* components and 5% of sqrt($|Zyx|^2$) for the *Zyy* and *Zyx* components of the impedance tensor. Error floors were set in this manner as the noise is most often on the electric fields, so noise on the Ex channel affects both the *Zxx* and *Zxy* estimates in the same absolute sense and similarly for noise on the Ey channel on *Zyx* and *Zyy*. Note that 5% error in impedance is equivalent to approximately 10% in apparent

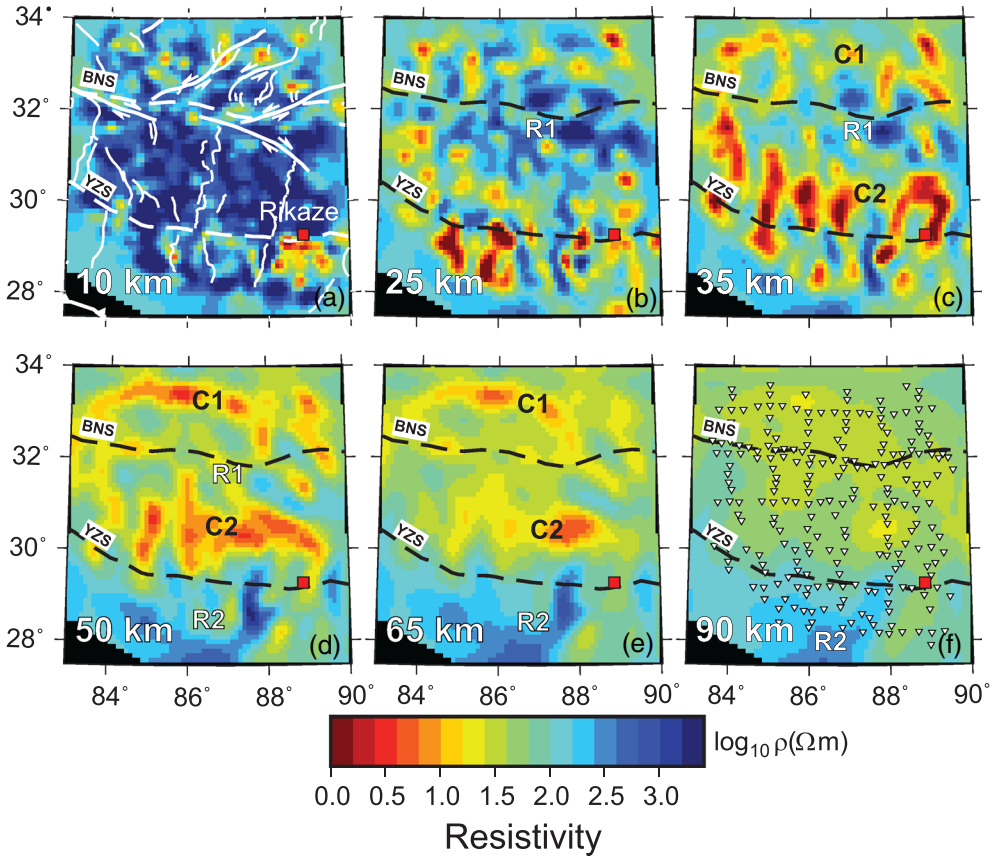

Figure 3. Resistivity maps at depths from 10 to 90 km. The inverted triangles show the location of MT sites. See Figure 1 for the descriptions for the surface structures superimposed. BNS: Bangong-Nujiang Suture zone; YZS: Yarlung-Zangbo Suture zone. The red square indicates the location of the city of Rikaze.

resistivity and 2.8° in phase. Absolute error floors for the geomagnetic transfer functions were set to 0.05 for *Tx* and *Ty* components.

Given the intensive computation and large memory requirements of 3-D inversions, the model mesh had to be limited to both a machine-manageable size and also to derive results in a reasonable time. Considering the nominal site spacing of 15 to 25 km of the SINOPROBE data, to model adequately the crust and upper mantle structures a uniform geographically oriented horizontal mesh size of 7.5 km on each NS and EW side was used for the study region.

While 3-D inversions do not have the inherent limitations of 2-D assumptions, small-scale shallow conductivity structures and topography still cause electric-field galvanic distortion in MT responses in 3-D problems (e.g., Jones, 2011; Käufl et al., 2020). To accommodate these, the complex topography of the plateau was modeled in the uppermost part of our model grid, with 27 thin layers each of 100 m in thickness. The dimensions of the vertical cells beyond this topography layer were allowed to increase exponentially with a factor of 1.2. These relatively thin layers allow the formation of small-scale conductivity heterogeneities in the inversion, which partly compensates for the galvanic distortions in the data. The final "core" mesh consisted of 90 × 85 × 70 cells (excluding air layers and padding cells to fulfill the electromagnetic boundary conditions), with a ~700 by 600 km model space covering the study region.

The inversion runs were carried out on a CUGB distributed-memory Linux cluster with 64 physical central processing unit (CPU) of a computer cores and a total memory of 576 GB. Based on the average resistivity of the crust and previous MT results in the study region (Unsworth et al., 2004; Wei et al., 2001), a 100 Ωm homogeneous half space was selected as both the start and prior model for the core region of the mesh. Details about the spatial parameters for the regularization scheme used in ModEM can be found in

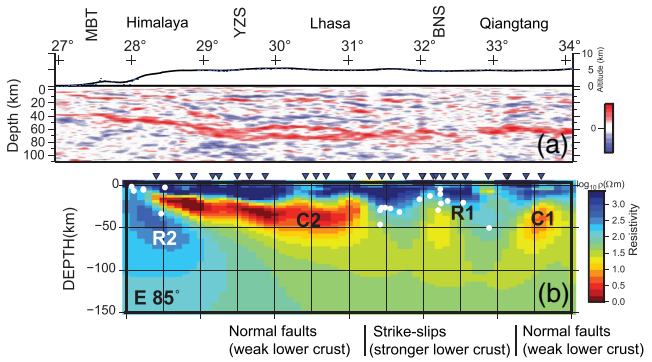

Figure 4. Comparison of (a) previous seismic receiver function image (J. Nabelek, 2009) in central Tibet and (b) corresponding N-S resistivity section at longitude of 85°E. White dots show the seismicity from 2000 to 2018 (Mw > 4.0) within a swath of 12 km from the section (seismicity data downloaded from http://www.csndmc.ac.cn). See caption of Figure 1 for the abbreviations of tectonic units.

the supporting information. The initial normalized root-mean-square (RMS) misfit for the starting model was 29.98. The preferred inversion model shown in Figures 3 and 4 was achieved after 378 iterations, resulting in an overall normalized RMS misfit of 1.81, with impedance RMS of 1.82 (equivalent to an average phase misfit of approx. 5°) and tipper RMS of 1.78 (meaning an average tipper misfit of approx. 0.09). The iterations are finished with a wall clock time of 5 days 8 hr, which translates into an ~6,800 core-hour computation cost.

The overall data fit is generally good to excellent, indicating that our preferred model is well constrained by the observed data and describes the observed data satisfactorily. Almost all the major features in the observed data are well reproduced by the response data calculated from our preferred model, for both the impedance tensors (supporting information Figures S1–S4) and induction vectors (supporting information Figures S5 and S6). Detailed comparison between the observed and the modeled response data can be found in the supporting information.

3.2. Discussion of the Preferred Model

As revealed in previous 2-D results from INDEPTH projects (Chen et al., 1996; Solon et al., 2005; Unsworth et al., 2005; Wei et al., 2001), our preferred model also images a relatively resistive upper crust (Figure 3a) and widespread conductive structures in the middle to lower crust of the doubly thickened Tibetan Plateau (Figures 3c and 3d). However, the resistivity maps do not show a coherent and uniform conductive lower crust, as suggested by earlier studies conducted along the graben systems. Instead, the lower crust is modeled with a far more complex geometry, with apparently N-S elongated conducting features (e.g., the conductor C2 in Figure 3c).

The most prominent features of our resistivity model are the two overall conductive features located in the Qiangtang (C1) and South Lhasa/North Himalaya (C2) terranes separated by a major resistive complex (R1) near the BNS. Interestingly, the conductive footprint of C2 seems to migrate to the north as depth increases (Figures 3b–3d), eventually to join with C1 at upper mantle depths (Figure 3f). This geometry and its depth variation are consistent with the dimensionality analyses, as the PT ellipses and induction arrows indicate a varying boundary location of the conductivity contrast at different periods, which is equivalent to different depths. Intriguingly, the conductive structures in C1 and C2 are well correlated with the location of surface graben zones and normal faults, whereas the resistive R1 feature lies only in the strike-slip deformation region. This pattern also coincides with that of Airy–Heiskanen isostasy gravity anomaly (Figure 1b), with the C1 and C2 anomalies corresponding well with the region with strong negative isostatic anomaly, whereas R1 is located beneath the region of zero or slightly positive anomaly.

On the other hand, a moderately resistive body (R2), which is best illustrated in a longitude cross section at 85° E (Figure 4b), is located in the lower crust and upper mantle of Himalaya terrane (Figures 3d–3f). This north dipping resistor spatially coincides approximately with the location of subducting Indian slab, as suggested by a seismic receiver function study (J. Nabelek, 2009). Similar features can be observed in all the longitudinal sections from our conductivity model (supporting information Figure S7). Curiously, the gently north dipping conductive layer C1 beneath the Himalaya and south Lhasa is also consistent with the lower crustal zone with decreased velocity (blue; Figure 4a). Moreover, resistor R1 in the vicinity of the BNS also overlaps with the region with an apparently "obscure Mohorovicic discontinuity" imaged between ~31.5° and 33°N (Figure 4a), as well as the shallower "unclear" Moho trace near BNS at ~88.5°E revealed by a deep seismic reflection survey (Lu et al., 2015).

Apart from the larger scale structures, our model also reveals finer scale (tens of kilometers) N-S aligning conductive features, located in the Lhasa and Qiangtang lower crust, that are spatially consistent with the loci of the longitudinal normal faults. However, the E-W dimension of these structures is comparable to the site "gaps" (e.g., the logistically inaccessible region between 87° and 88°E in south Lhasa terrane).

With our site layout, we test whether it is possible that these structures are artifacts determined by station positions and the regularization mechanism.

A series of inversion tests were performed with MT transfer functions generated from various synthetic model features to test if those features can be recovered with the actual site layout. We also try to mimic anisotropy with isotropy at a finer scale than can be resolved with our data (see supporting information for details). The results show that even the features that are almost completely located in the "gaps" between the stations (supporting information Figures S8a and S8e) and features oblique to the general site orientation (supporting information Figures S8c and S8g), can be well resolved by the inversion scheme with the current site layout. This implies that the orientation of the fine-scale features in the preferred model is unlikely to be controlled by site spacing but is a representation of true subsurface structure. However, N-S anisotropic features (simulated by very fine thin stripes that cannot be resolved by isotropic methods) could still produce a similar, fine N-S aligning response as in our study (supporting information Figures S9a and S9h). Unfortunately, to-date general anisotropic inversions are still far from practical in 2-D, not to mention 3-D cases (e.g., Baba et al., 2006; Evans et al., 2005; Pek et al., 2011; Pek & Verner, 1997). As such, we have to limit our modeling to isotropic conductivity.

It is generally believed that the seismically slower and electrically conductive lower crust in the Tibetan Plateau can be attributed to partial melts and/or aqueous fluids (S. Li et al., 2003; Makovsky & Klemperer, 1999; Nelson et al., 1996), which significantly lowers crustal strength (Le Pape et al., 2015). Indeed, the epicenters of earthquakes projected onto our resistivity sections are mostly located in the resistive structure, or the boundary of conductive structures (Figures 4b and S7). The conductive lower crust in the south Lhasa and Qiangtang terranes with little seismic activity could indicate that the rock is simply too weak and/or ductile to generate earthquakes by brittle failure. The deep earthquakes near the BNS, on the other hand, suggest that the lower crust is stronger or near the brittle state for the strike-slip zone (Figure 4b).

The electrical conductivity of the deep crust has long been used to estimate the fluid fraction and viscosity, based on laboratory experiments to calibrate the relationships within (Brown, 2001; Pommier, 2013). Our discussions below will focus on applying constrains to rheology with the conductivity model, which further aids understanding the surface deformation of the central Tibetan Plateau.

4. Rheology Constraints From Conductivity Model

4.1. Bridging Conductance and Fluid Fraction

As with most regularized geophysical inversions, the ModEM MT inversion scheme tries to find a model that fits the data and at the same time keeps the spatial variation of different layers small (aka smooth), because the prior model was smooth (uniform in the core region) and regularization was to the prior. As a result, MT data generally have a better resolved estimate of the conductance of a certain layers, in particular conducting ones, instead of the actual resistivity itself (Jones, 1992; Weidelt, 1985). It is therefore advantageous to estimate the fluid fraction (and hence viscosity) through effective bulk conductivity derived from conductance (Le Pape et al., 2015; Rippe & Unsworth, 2010). Conductance can be calculated by integrating the $S = h/\rho$, where S (in Siemens, S) is the total vertically integrated conductance of the layer, h (in meters, m) is the thickness of the layer, and ρ (in Ωm) is its (isotropic) resistivity, of each discrete layer for the depth range considered.

The integrated conductance of the middle to lower crust (25–65 km) calculated from our preferred resistivity model is shown in Figure 5. Similar to the implication from our resistivity model, the loci of the high conductance zones (over 10,000 S) correlate well with the graben distributions in Lhasa, whereas the low conductance structures (<3,000 S) mainly concentrate in the vicinity of the BNS and south Himalaya. For a "partial melt" condition, which is appropriate for Tibetan mid/lower crust, estimation of melt fraction requires the use of two-phase media formalisms, such as Hashin-Shtrikman bounds or Archie's law (ten Grotenhuis et al., 2005). According to Archie's law, the fluid percentage Φ can be estimated based on

$$\sigma_{eff} = c\Phi^{n}\sigma_{f} \tag{1}$$

where σ_{eff} is the effective conductivity, which is calculated from the integrated conductance and the layer

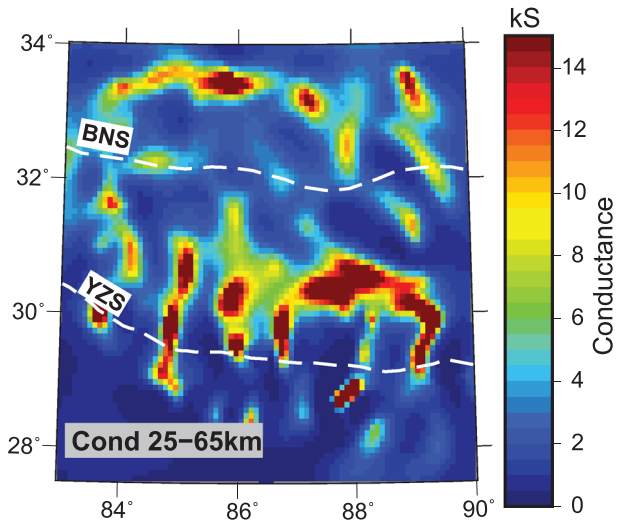

Figure 5. Vertically integrated conductance map for depth from 25 to 65 km of the preferred resistivity model. BNS: Bangong-Nujiang Suture zone; YZS: Yarlung-Zangbo Suture zone.

thickness (40 km for the middle to lower crust in our case). σ_f is the fluid phase conductivity, with $c = 1.30$ and $n = 1.47$ the empirical constants for olivine melts proposed by ten Grotenhuis et al. (2005). However, one problem with applying Archie's law is that it does not take into account surface conductivity or grain boundary conduction. The grain boundary proton diffusion is orders of magnitude faster than that of the lattice diffusion, which significantly enhances the "conductivity" of the material and may provide a way to explain the highly conductive lower crustal and upper mantle anomalies revealed by MT studies (Jones, 2016).

Apart from surface conductivity, conventional Archie's law also does not account for the conductivity of the rock matrix (σ_r is assumed to be zero in conventional Archie's law). Hence, herein we include in addition the results from applying a more general empirical formula, namely, the modified Archie's Law (Glover et al., 2000), to estimate the fluid percentage from conductivity in the two-phase medium given by

$$\sigma_{eff} = \sigma_r(1-\Phi)^{(\log(1-\Phi^m)/\log(1-\Phi))} + \sigma_f \Phi^m, \quad (2)$$

where σ_r and σ_f are the conductivity of the solid and fluid phases, while Φ remains the fluid fraction. m is the cementation exponent, which measures the electrical connectivity of the fluid phase in the porous medium. The cementation exponent m is 1.0 when the fluid phase is considered highly interconnected, whereas $m = 2.0$ describes an isolated fluid distribution (Glover et al., 2000).

To determine the fluid fraction Φ it is essential to know, or at least constrain, the conductivities of the fluid and rock matrix phases: σ_f and σ_r. As σ_r is normally orders of magnitude smaller than σ_f, effective conductivity is dominantly controlled by the fluid conductivity, especially for lower temperature environments. However, a wide range of fluid conductivity has been assumed in previous studies, from a moderate value of 2–4 S/m (Le Pape et al., 2015) in northern Tibet to a very high value of 5–20 S/m in eastern Tibet (Bai et al., 2010). Recent studies even reported that the conductivity of saline fluids can reach extreme values like 10–100 S/m (Sakuma & Ichiki, 2016; Sinmyo & Keppler, 2017); the theoretical maximum for supersaturated saline fluids is of order 400 S/m (H. Guo & Keppler, 2019; Nesbritt, 1993). It should be noted that the phase conductivities are determined by a series of parameters, such as melt/fluid composition, temperature, pressure, and water content. Therefore, instead of choosing arbitrary values, here we estimate the conductivities of the rock and fluid phases by those parameters. It is therefore preferable that the parameters are constrained by independent geoscientific studies, as discussed below.

4.2. Temperature and Pressure

The coverage of surface heat flow measurements on Tibetan Plateau is very limited, with some extreme values (>150 mW/m^2) that are mostly recorded in anomalous regions or geothermal fields. Still, it is generally accepted that a moderately high heat flow of ~60–80 mW/m^2 is valid for southern Tibet (Tao & Shen, 2008). If an average geothermal gradient of 27 °C/km is assumed (C. Wang et al., 2014), the upper boundary of the depth range we are interested (25 km) will be around 685 °C. Previous geothermal numerical simulations suggest a ~750 °C lower crustal temperature in the southern Lhasa terrane (Jiménez-Munt et al., 2008), and ~800 °C in the northern Lhasa terrane (C. Wang et al., 2013), which is also consistent with the estimation (32 km depth) from seismic detection of α-β quartz transition at the BNS (Mechie et al., 2004).

On the other hand, if densities of 2,700 and 3,050 kg/m^3 are assumed for the upper and lower crust, respectively (Haines et al., 2003), the pressure at the range of 25–65 km depth should be around 0.7–1.8 GPa. Here we take the values at ~35 km depth, where the conductive anomalies are most pronounced, with a temperature and pressure of about 800 °C and 1.0 GPa, respectively (P. Nabelek & Nabelek, 2014; C. Wang et al., 2013).

4.3. Water Content

Water plays a crucial role in the melting process, as it dramatically lowers the temperature required for partial melting (Thompson & Connolly, 1995). Note that our conductive anomalies of interest (C1 and C2) lie mostly in the depth range of the middle to lower part (25–65 km) of the doubly thickened crust of the Tibetan Plateau. Under the high temperature discussed above, aqueous fluids in this depth range would trigger fluid-present partial melting and consequently dissolve into the melt (see, e.g., Le Pape et al., 2015, and references therein). As such, we will not consider the case that the conductive anomalies are solely caused by aqueous fluids. On the other hand, partial melting could still initialize without pore/intergranular manner (Wannamaker, 1986). Dehydration reactions of common crustal minerals start to occur at relatively low temperatures for hydrated minerals (e.g., 650–750 °C for biotite, amphibole or muscovite; Weinberg & Hasalová, 2015) and provide the necessary water to initiate partial melt. Indeed, samples from the middle to late Cenozoic magmatic events show >4% water content, which is believed to resulted from dehydration melting (R. Wang et al., 2014).

As the southern part of Tibetan plateau has not experienced any large-scale magmatic events since the Miocene, the majority of water in the melts should remain trapped in the lower crust. Moreover, the subducted Indian lithospheric mantle beneath the present-day Lhasa terrane is considered to be anhydrous eclogite, which cannot supply additional pore/intergranular water for the lower crust melts (P. Nabelek & Nabelek, 2014). It is therefore reasonable to assume that the melts in the present-day lower crust maintain a similar level of water content as observed in the middle to late Cenozoic volcanic eruptions.

Still, it is no simple task to determine the amount of water present in the melts in our scenario. Experimental constrains suggest bound H_2O content of 5–6 wt.% (Patino Douce & Harris, 1998) or >6 wt.% (Hashim et al., 2013) for water dissolved in Himalayan granite magmas in the late Oligocene to Miocene times. Recent studies show that dehydration melting may result in melt water content of as high as 6%–8% (J. Chen et al., 2018) in the southern Tibetan Plateau. Conductivity models with laboratory constraints also predict a similarly high level of water content (7%–9%) in the lower crust (Comeau et al., 2016; Laumonier et al., 2014). Moreover, as magmas rise through the crust and solidify, aqueous fluids are released under the reduced pressure (J. Chen et al., 2018), resulting in a lower bound water content than at the melt loci. Hence, we consider the constrains from the laboratory experiment as a lower limit.

The upper limit, on the other hand, is constrained by the initial water saturation of rocks, governed by temperature and pressure (Weinberg & Hasalová, 2015). Experiments show that water content dissolved in melts can reach as high as at least 10 wt.% at 1 GPa and 900 °C (dacite, Prouteau et al., 1999) or 15 wt.% at 1 GPa and 1000 °C (rhyolite, Duan, 2014). Here we take an upper limit value of 9 wt.% for southern Tibet, as suggested by Guo et al. (2018).

4.4. Melt Fraction Estimation

Accounting for temperature, pressure, and water content effects altogether, granitic melt conductivity σ_f can then be calculated according to a generalized formula constrained by experimental data (X. Guo et al., 2018):

$$\log\sigma_f = 3.205(\pm0.067) - 0.102(\pm0.016)w - \frac{4228.5(\pm83.2) - 354.7(\pm18.1)\mathrm{w} + 694.6(\pm37.8)\mathrm{P}}{\mathrm{T}} \quad (3)$$

where w is the water content (in wt.%), P is the pressure (in GPa), and T is the temperature (in K). J. Chen et al. (2018) developed a similar empirical model for the estimation of the melt/fluid conductivity using the Arrhenius equation. Figure 6a shows the calculated fluid conductivity from both the Guo et al. (2018) and J. Chen et al. (2018) formulae under the middle to lower crustal conditions of the Tibetan Plateau (1 GPa). The estimated σ_f values from the two approaches are very similar in our target temperature range (~800 °C), except for dry melt. As in the previous discussion, if 6–9 wt.% water content is adopted for the partial melts, with the above mentioned thermal and pressure state (~800 °C and 1 GPa), the melt conductivity would range from ~1.12 to 1.96 S/m, considering both formulations, which is well less than a factor of two different.

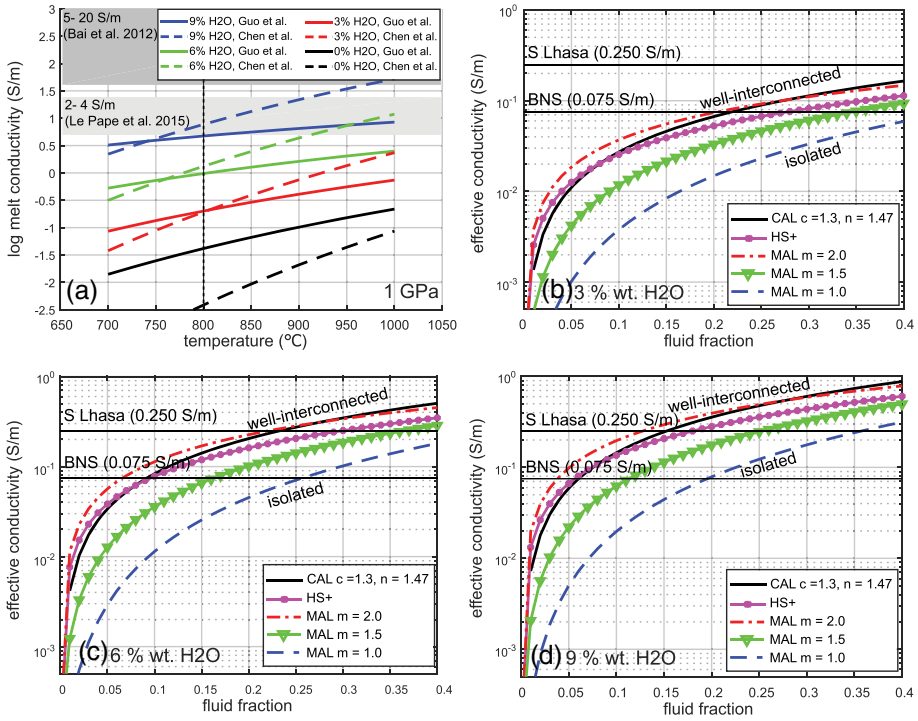

Figure 6. (a) Melt conductivity calculation with various water contents and temperatures at 1 GPa pressure from formalisms from Guo et al. (2018) and J. Chen et al. (2018); (b–d) the fluid fraction estimation with 3%, 6%, and 9% wt. water content at ~800 °C and 1.0 GPa with conventional Archie's law (CAL, ten Grotenhuis et al., 2005), modified Archie's law (MAL; Glover et al., 2000), and Hashin-Shtrikman upper bound (HS+; Hashin & Shtrikman, 1963). BNS: Bangong-Nujiang Suture zone; YZS: Yarlung-Zangbo Suture zone. See text for details.

Similarly, the conductivity of the solid phase σ_r can be calculated using an empirical formula (Equation 3) of Hashim et al. (2013). However, under the temperature (~800 °C) of our target depth, the rock matrix conductivity is only ~9.75×10^{-4} S/m, which would only contribute a minor fraction of the bulk conductivity unless the fluid fraction is small (<1 wt.%).

Now that we have both σ_r and σ_f constrained within reasonable and realistic bounds, the melt fraction can be estimated with Archie's law, in both the conventional and modified form (Figures 6b–6d). The Hashin-Shtrikman upper bound is also used (Hashin & Shtrikman, 1963) to establish a reference for the effective conductivity in a relatively well-interconnected case. With smaller melt fractions (<20%), the results from conventional Archie's law are consistent with those from the Hashin-Shtrikman upper bound (HS+), as noted by Waff over 45 years ago (Waff, 1974). Particularly, CAL results are less conductive than the HS + for low melt fractions (<~10%) but more conductive with higher fractions (>~10%). However, as the melt fraction increases (>30%), the effective conductivity from CAL (ten Grotenhuis et al., 2005) starts to exceed even the values from well-interconnected fluid phase ($m = 1.0$) with the modified Archie's Law. This indicates that the parameters proposed by ten Grotenhuis et al. (2005) ($C = 1.30$, $n = 1.47$) are not appropriate for higher fluid fraction conditions. Nevertheless, as the melt is less likely to be well interconnected with lower fractions (and vice versa, as observed in ten Grotenhuis et al., 2005), we consider the CAL model from ten Grotenhuis et al. (2005) a better estimate in our case.

As shown in Figures 6c and 6d, the conductive graben region (with conductance of ~10,000 S and effective conductivity of 0.25 S/m) should contain 15% to 23% melt phase with the σ_f estimation. The relative resistive strike-slip region near the BNS (<3,000 S or 0.075 S/m) would suggest a much smaller volume of fluid fraction (melts), lower than 6.5% to 9%. Those values are consistent with previous estimates in southern Lhasa (10%–23%) and northern Lhasa (4%–9%) (Rippe & Unsworth, 2010).

Partial melts could significantly reduce the viscosity of rocks in various ways (Renner et al., 2000). Laboratory experiments indicate that even a small fraction of 5%–10% melts could reduce the strength of

granite by an order of magnitude (Rosenberg & Handy, 2005), while a melt content of 20% could increase the strain rate by approximately 2 orders of magnitude for dunites (Bürgmann & Dresen, 2008). The lower conductance and melt fraction in the strike-slip region near the BNS implies a relatively stronger lower crust, whereas the lower crust of the graben region consists of much weaker structures, due to the higher melt percentage.

4.5. Rheological Analysis

As conductivity is the most sensitive observable geophysical parameter to fluid and melt phases, extensive effort has been made to derive a quantitative relationship between conductivity and viscosity (e.g., L. Liu & Hasterok, 2016; Pommier et al., 2013; Rippe & Unsworth, 2010; Schilling & Partzsch, 2001). Notwithstanding these attempts, viscosity values are still not well constrained from electrical conductivity in a very deep lower crustal environment, as the laboratory viscosity measurement in those studies were mostly conducted at atmospheric pressure (Schilling & Partzsch, 2001) or upper crustal level pressure (Hashim et al., 2013).

Pommier et al. (2013) proposed an empirical formula based on laboratory studies to link the melt viscosity and electrical conductivity for certain combinations of temperature, melt composition, and water content. Comeau et al. (2016) successfully adopted Pommier et al.'s (2013) approach to estimate the viscosity of melts in the lower crustal magma chambers beneath the Uturuncu Volcano. However, this relationship is mostly focused on the calculations for partially molten rocks with very high melt fraction (>70%; Pommier et al., 2013). The estimated viscosity at upper crustal (10^{11}–10^{12} Pa·s; Hashim et al., 2013) and lower crustal (10^{11}–10^{12} Pa·s; Comeau et al., 2016) levels is also many orders of magnitudes smaller than the lower crustal values (10^{18}–10^{19} Pa·s) for the Tibetan Plateau from numerical modeling studies constrained by surface velocity and strain rate (Chen et al., 2017; Jamieson et al., 2004).

Instead of directly computing rheology from conductivity, Rippe and Unsworth (2010) proposed a method that links viscosity to the partial melt fraction in a "channel flow" due to the pressure gradient from gravitation. Electrical conductance is used to predict the melt fraction, which is, in turn, used for the estimation of rheological material constant of a viscous flow. This requires the existence of a crustal channel flow (Couette or Poiseuille type), as the strain rate of such a flow is needed to calculate the effective viscosity using this method. The method cannot be applied to regions that do not support such channel flows (e.g., mechanically strong regions with little melt fraction or flat regions that have no topography contrast and pressure gradient). Unfortunately, with the complex geometry of the conductivity structures revealed, it is difficult, if not impossible, to model the conductive anomalies as simplified channels for viscous flow.

As the electrical conductivity and viscosity are both related to similar controlling factors and formulae, L. Liu and Hasterok (2016) proposed an empirical framework that relates the electrical conductivity (resistivity) to mechanical viscosity:

$$\frac{\eta_{eff}}{\eta_0} = C_0\left(\frac{\rho}{\rho_0}\right)^{C_1} \tag{4}$$

where η_{eff} is the estimated effective viscosity, $\eta_0 = 10^{20}$ Pa·s is the reference viscosity, ρ is the measured resistivity, while $\rho_0 = 100$ Ωm is the reference resistivity. C_0 is a factor that determines the viscosity of the reference resistivity ρ_0, with typical values range from 0.5 to 8.0 (L. Liu & Hasterok, 2016). For example, $C_0 = 2.0$ indicates that a 100 Ωm resistivity value represents a viscosity of 2.0×10^{20} Pa·s. In other words, C_0 greater than identity (1) indicates an overall stronger rheology, and vice versa. On the other hand, C_1 controls the maximum contrast of the regional viscosity structure. With a resistivity contrast of three orders of magnitude, a small C_1 (e.g., 0.35) leads to a viscosity variation of only 1 order of magnitude, whereas $C_1 = 2.0$ results in a magnitude difference of six orders. The geodynamic study with crustal viscosity informed from magnetotelluric resistivity model shows a promising match with the observed surface stress (Murphy et al., 2019).

However, it is worth noting that not all the conductive phases are closely related to mechanically weak structures, especially for the shallow part of the crust. This could also explain the fact that the rheology models computed with this method are less consistent with the corresponding mechanical models in the upper

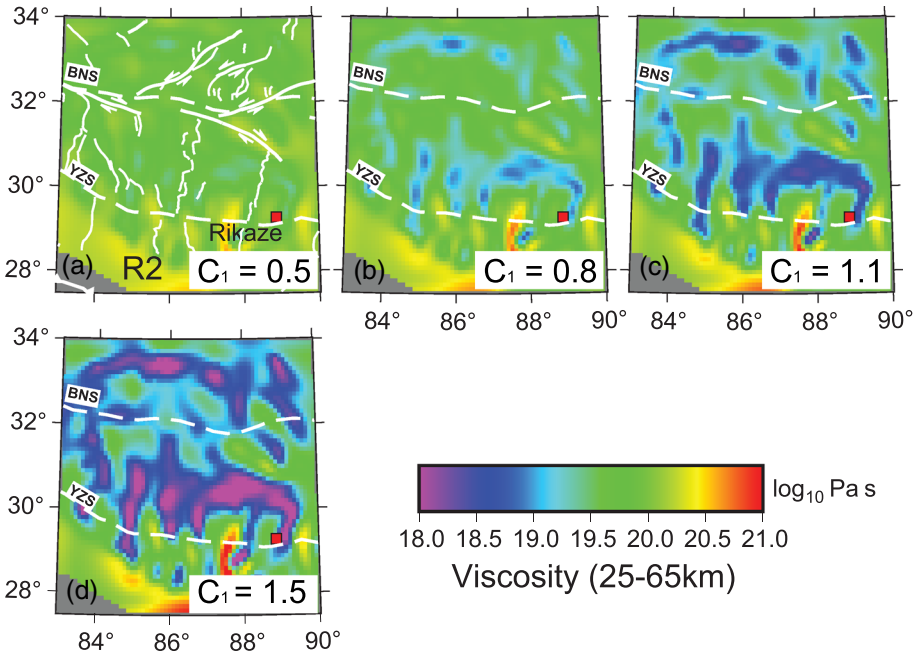

Figure 7. Viscosity maps of the middle to lower crust derived from conductivity. (a–d) Viscosity calculated by L. Liu and Hasterok (2016) formulism with coefficients $C_0 = 2.0$ and C_1 from 0.5 to 1.5. See text for detailed information.

crust (L. Liu & Hasterok, 2016). Moreover, without the systematic validation of numerical geodynamic modeling, the selection of the coefficients is unconstrained and becomes somewhat arbitrary and will not be accurate. With all of these uncertainties in mind, here we only apply the method to the middle to lower crust, in order to obtain a preliminary rheology constraint of our study region. Additionally, as explained in section 4.1, we use the calculated conductance map from 25 to 65 km to compute the effective resistivity and the corresponding viscosity distribution (Figure 7).

Since the subducting Indian plate (the resistive anomaly R2 in Figures 3 and 4) is believed to be relatively cold and rigid comparing with the Tibetan lower crust, here we assume the India plate (>100 Ωm in resistivity) to be slightly stronger than average lower crust (2.0×10^{20} Pa·s; Shinevar et al., 2015). As such, we keep the parameter C_0 to 2.0. We also tested various C_1 values from 0.5 to 1.5, which result in an overall spatial viscosity variation with about 1 (~2×10^{19} to 3×10^{20} Pa·s,) to 5 (~3×10^{16} to 3×10^{21} Pa·s) orders of magnitude. The value $C_1 = 1.1$ is preferred, as the resulting effective viscosity is ~2×10^{18} to 2×10^{19} Pa·s for the graben region in south Lhasa, similar to the assumptions of numerical geodynamic studies (Bischoff & Flesch, 2018) and the results from crustal flow analysis (Rippe & Unsworth, 2010). This is also well consistent with the low midcrustal viscosity value (<$1 \times 10^{18.5}$ Pa·s) constrained by interseismic deformation data near active faults on the Tibetan plateau (DeVries & Meade, 2013). The effective viscosity for the strike-slip zone near the BNS, on the other hand, ranges from ~2×10^{19} to 2×10^{20} Pa·s. While weaker than the subducted Indian plate, this is about an order of magnitude higher than within the graben region. Although we have insufficient data to constrain structures further to the north, the higher conductance in the graben region in the Qiangtang block leads to a lower viscosity value (~3×10^{18} Pa·s), which also suggests a much weaker lower crust compared to that beneath the BNS. Our lower crust viscosity model, as provided in the supporting information, may offer a good starting point for more robust, future geodynamic modeling studies.

We should also note that the estimated rheology distribution is by no means homogeneous within the graben and strike-slip regions. Small-scale weak zones (~5×10^{18} Pa·s) can be observed near the BNS (Figure 7c), which is approximately spatially consistent with locations the low velocity anomalies in the crust (Zhou et al., 2019). Similarly, isolated high viscosity anomalies can also be found in the overall weak south Lhasa region. Those unevenly distributed viscosity anomalies may further suggest localized weaker/stronger area characterized by heterogeneous viscosity distributions, where stresses tend to concentrate.

Despite our simplified derivation from conductivity to rheology, the complex viscosity pattern and pronounced melt fraction difference would nevertheless suggest a starkly contrasting rheology distribution in the lower crust of the Tibetan Plateau. This, along with previous rheology studies in the Tibetan Plateau, raises the question as what kind of tectonic events could form such a peculiar distribution. Also, more importantly, could this rheology distribution contribute to the formation of the enigmatic surface deformation of Tibetan Plateau?

5. Discussion

5.1. Tectonic Scenarios

The southern part of the Lhasa block experienced widespread basaltic to andesitic magmatism during early Cenozoic times. Aside from calc-alkaline volcanism, the Lhasa block has been characterized with potassic and ultrapotassic intrusions since the Oligocene (Nomade et al., 2004). Those intrusions are believed to be related to metasomatism in the lower crust or lithospheric mantle, which suggests convective thinning or removal of mantle lithosphere (C. Liu et al., 2011). Curiously, the strike-slip zone near the BNS is barren in Cenozoic magmatism, with almost no samples after the Miocene (Nomade et al., 2004), whereas the normal fault zone in the Qiangtang terrane is again characterized with younger volcanism since the Pliocene (Q. Wang et al., 2016).

Along with the magmatic activity, E-W extension of the grabens began to initiate in the middle to late Miocene in the south Lhasa terrane (Huang et al., 2016), which coincides with the uplift of southern Tibet as suggested by thermo-chronometry (Lee et al., 2011). The strike-slip faults, on the other hand, formed in Miocene times (~8 Ma) in the central part of the Tibetan Plateau (Yin & Taylor, 2011) and have also similar ages to that of the grabens. Geophysical studies reveal a deep Moho discontinuity in the present-day Lhasa terrane that could result from a significant crustal thickening since the Miocene (Styron et al., 2015).

Combining the existing geophysical and geochemical information, we propose a tectonic process that explains our conductivity model. In this scenario, possibly triggered by the breakoff or rollback of the subducting Indian Plate, hot mantle material started to rise since the Oligocene, resulting in convective thinning of lithospheric mantle (C. Liu et al., 2011). The hot upwelling material interacted with the lithosphere and induced metamorphic dehydration/devolatization which introduced fluids in the lower crust and upper mantle (Comeau et al., 2018). These fluids, in turn, triggered partial melting, weakening the local mechanical strength and producing the potassic and ultrapotassic lavas in the Miocene (Figure 8a). However, as subduction of Indian slab continued to the north, the upwelling window of mantle material gradually closed, ceasing the volcanic activity in the Lhasa terrane after ~5 Ma. Still, part of the melts remain even after the window closed shut (Figure 8b), as the frictional heat of the underthrusting Indian slab maintained high temperature in the lower crust (P. Nabelek & Nabelek, 2014). Therefore, those partial melts are imaged as lower crustal conductive structures in the southern part of the Lhasa terrane, as shown in Figure 8c. The underthrusting Indian plate also contributes to the thickening of southern Lhasa crust and further supports higher topography than found in the BNS region (Styron et al., 2015).

On the other hand, the upper mantle (and lower crust) near the BNS could well be depleted during the intense volcanic activities during the Jurassic–Cretaceous amalgamation of the Lhasa and Qiangtang terranes (Zhu et al., 2016), thus not be able to give rise to young melts in the Miocene. Not affected by the large portion of melts as in southern Lhasa, the lower crust remained stronger and is imaged as a resistive anomaly (R1 in Figure 8c) near the BNS, which also overlaps with the lower crustal high velocity zone revealed by INDEPTH active seismic data (Haines et al., 2003). The lower crust could have experienced partial eclogitization, which formed the obscure Moho imaged near the BNS region (Lu et al., 2015; J. Nabelek, 2009). This is because the velocity difference between a partially eclogitized lower crust and uppermost lithospheric mantle (peridotite) can be insignificant (7.5 and 8.0 km/s for *P* waves; e.g., Kukkonen et al., 2008) and virtually invisible for most seismic investigations. Deep-seated eclogitization can also account for the weak positive Airy–Heiskanen isostasy gravity anomaly (Figure 1b) and relative low elevation in the vicinity of the BNS, comparing with the higher elevation in the Lhasa and Qiangtang terranes, with strong negative isostatic anomaly (Figure 1b). Crustal eclogite (high density) may compensate for the extra buoyancy from the thick crust in the Plateau and lead to a flat topography and less negative isostatic anomaly.

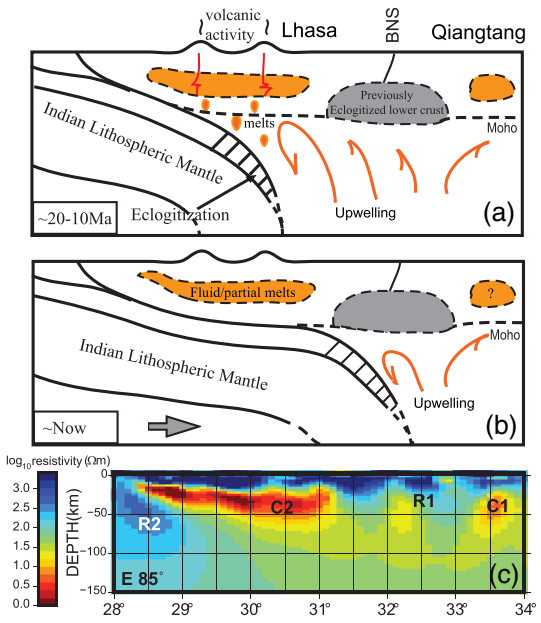

Figure 8. (a and b) Schematic illustration of the tectonic evolution of the study region. (c) N-S resistivity section at longitude of 85°E. See caption of Figure 1 for the abbreviations of tectonic units.

5.2. Shaping the Surface Deformations

The rheology of the crust plays a crucial role in the building of surface topography and deformation (Klemperer, 2006). However, previous hypotheses on the rheology and geodynamics of Central Tibet are mostly based on geophysical observations from profiles, mostly along N-S grabens, with limited coverage. Our MT data and 3-D conductivity model establishes the first regional constraints on the melt fraction and viscosity of the lower crust for the whole of the central part of the Tibetan Plateau. Our preferred MT inversion model images conductive lower crustal structures beneath the graben regions in the Lhasa and Qiangtang terranes and resistive structures near the conjugate strike-slip zone along the Bankong-Nujiang Suture (Figures 3 and 4). The derived rheology model suggests a peculiar viscosity distribution around the BNS; a relatively strong lower crust is sandwiched by E-W extending weaker regions with low viscosity and partial melts in the Qiangtang and South Lhasa terranes (Figure 7c).

A tempting interpretation for this pattern is to attribute the two "weak zones" as the lower crustal channels, as proposed by previous "eastward crustal flow" models (Royden et al., 1997; Unsworth et al., 2005). Indeed, lateral crustal flow could explain the expansion of grabens and eastward surface displacement (Gan et al., 2007). However, instead of continuous E-W extending "channels," as is expected in an eastward flow case, in sharp contrast the lower crust conductance map clearly shows N-S aligned structures in both the Qiangtang and Lhasa terranes. Those smaller scale N-S conductors also approximately correspond to the loci of surface normal faults. Curiously, the N-S conductive features are similar to those revealed in northern and eastern Tibet (H. Dong et al., 2016; Le Pape et al., 2012), which argue against the model of east-west channel flow in the lower crust. Alternatively, the previously proposed "extensional extrusion" model (H. Dong et al., 2016) remains consistent with the expansion of the graben regions. In that model, the E-W extension of the lower crustal ductile material leads to the brittle failure of the upper crust and the opening of the grabens. However, the model did not consider the conjugate strike-slip faults near BNS.

Therefore, here we expand our "extensional extrusion" mechanism proposed in H. Dong et al. (2016) under the new rheological constraints of central Tibet, with the view to reconcile its complex surface deformation. As the northward subduction of India continues, the crust experiences N-S compressional and E-W extensional stresses. The resistive upper crust and the highly conductive lower crust imaged in the graben zones (Figures 3 and 4) indicate a thin and brittle upper crust underlain by a weak/ductile middle to lower crust (Figure 7). A N-S compression would cause the weak lower crust material to expand in the other two (vertical and E-W) directions (Figure 9). This could explain the fact that the central parts of the graben systems had been continuously uplifted and remain topographically high (Kapp et al., 2008). The upward expansion (or the subsidence by gravitation) of the ductile lower crust would result in a vertical primary stress in the upper crust. According to Anderson's "standard" relationship between stress and fault types (Simpson, 1997), this stress pattern may induce localized E-W extensions and N-S directed normal faults, as observed in the graben zone. This correlates well with the numerical simulation experiments for central Tibet (Pang et al., 2018) that show a weak lower crust giving rise to the E-W opening of the graben systems. In a similar manner as in the eastern Tibet (H. Dong et al., 2016), these local E-W extensions would accumulate and produce the eastward surface velocity field (Gan et al., 2007).

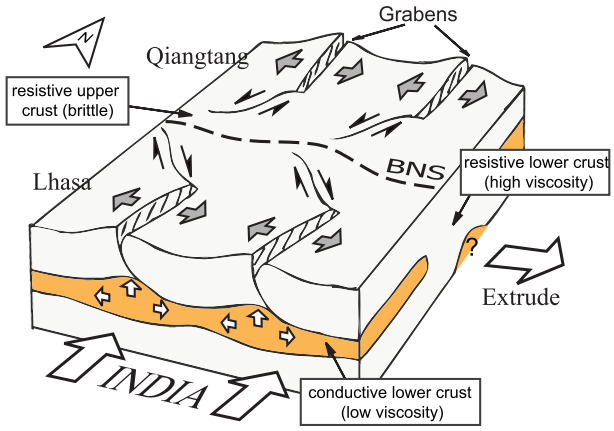

Figure 9. Schematic illustration of the extensional extrusion process in central Tibet (not to scale). The orange shades show the distribution of conductive lower crustal anomalies and possible weak (low viscosity) structures. See caption of Figure 1 for the abbreviations of tectonic units.

On the other hand, the generally resistive crustal structures imaged near BNS (Figures 3 and 4) would suggest a thicker brittle upper crust with a much stronger/less ductile lower crust (Figure 7c). In that case, the primary stress will be N-S directed, which could result in shear failures, creating strike-slip style faults near the BNS. The stress state variation (vertical primary stress vs. N-S primary stress) is consistent with the normal to strike-slip transition of seismic focal mechanisms from south Lhasa to the BNS (Styron et al., 2011). Furthermore, with the eastward surface movement accumulated in the graben zone, the graben zone should be "dragging" the north and south boundary of the strike-slip zone to the east (Figure 9). This could facilitate the generation of the V-shape "paired general-shear" faults, instead of the conventional Anderson-style X-shaped strike-slip faults (Yin & Taylor, 2011). This would also explain the fact that all of the major conjugate strike-slip systems are NE/SE directed (east facing <) instead of NW/SW manner. These, together with the N-S compression upon the "<" shaped conjugate strike-slip zone, can cause the landmass to be extruded to the east (Figure 9), which also explains the fast-eastward surface motion in the vicinity of the BNS (Gan et al., 2007).

To summarize, our integrated magnetotelluric and geodynamic interpretation suggests that the surface deformation in central Tibet can be explained by a contrasting regional stress state, caused by the complex crustal rheology. Under the regional N-S compressive stress, the conductive/weak lower crustal structures imaged beneath Lhasa and Qiangtang lead to the E-W extension of the graben systems. With the resistive/strong crustal structures imaged between the Lhasa and Qiangtang terranes, the extension process could also contribute to the formation of the strike-slip faults along the BNS and the eastward extrusion of the crustal material.

An alternate theory involving basal slide from lower crustal or asthenospheric flow beneath the BNS can also explain the generation of the conjugate faults (Yin & Taylor, 2011; Zhou et al., 2019). Particularly, the major difference between our model and that model is the driving force of the proposed geodynamic displacement. Although our geodynamic model does not reject the possibility of such an flow, a recent seismic study (J. Li & Song, 2018) and our MT results cannot image a pronounced lower crustal velocity or conductivity anomalies that support the presence of continuous lower crustal flow along the BNS. Still, the deeper mantle-level conductive features near the BNS (Figures 3f and 4b) could indicate a mechanically weaker zone in the upper mantle. This could act as a transitional boundary that allows the strike-slip zone to be extruded laterally. It should also be noted that real-world structures often have no clear boundary (as illustrated in Figure 9) between the strike-slip and normal deformations. Future investigations on the "transform" structures between the two may help improve understanding this complex, ongoing process.

6. Conclusions

In this study, we present the results from a 3-D magnetotelluric study covering the central part of the Tibetan Plateau. The derived high-resolution 3-D lithospheric conductivity model, along with experimentally calibrated constraints bridging conductivity and melt fraction, provide a way to constrain the subsurface rheology. Though preliminary, the viscosity model informed from conductivity reveals contrasting lateral rheology differences in the lower crust. These rheological differences could have led to the strong surface deformation patterns, namely, the conjugate strike-slip faults near the BNS and the N-S aligning grabens in the Lhasa and Qiangtang blocks of Tibet. Consistent with recent geophysical and geochemistry observations, our expanded "extensional extrusion" model explains the conductivity image and the complex surface deformations resulted from the stress and rheological state. The accumulated local E-W extensions in the graben zone, along with the lateral extrusion in the conjugate fault zone, could support the general eastward surface motion observed in central Tibet.

At this point the detailed upper crustal structure is not well understood given the limitation of the current station distribution, especially for the region near the BNS. Also, our data set does not have coverage to the north of 34°N in the Qiangtang terrane; this demands future surveys with denser station distribution. Our geodynamic model at the current stage is conceptual and qualitative.

Data Availability Statement

The supporting information files for this study can be found online (https://doi.org/10.17632/svwdw67tfv.2).

Acknowledgments

This study was supported by project SINOPROBE and NFSC young scientist funding 41504062 to H.D. Special thanks go to the field crews and students; without them, this study could never have been undertaken. Discussion with Danping Yan and Dicheng Zhu helped improve the development of our tectonic interpretation. The authors appreciate the comments and suggestions from the editors and two anonymous referees that helps improving the manuscript.

References

Baba, K., Chave, A. D., Evans, R. L., Hirth, G., & Mackie, R. L. (2006). Mantle dynamics beneath the East Pacific Rise at 17°S: Insights from the Mantle Electromagnetic and Tomography (MELT) experiment. *Journal of Geophysical Research*, *111*, B02101. https://doi.org/10.1029/2004JB003598

Bai, D., Unsworth, M. J., Meju, M. A., Ma, X., Teng, J., Kong, X., et al. (2010). Crustal deformation of the eastern Tibetan plateau revealed by magnetotelluric imaging. *Nature Geoscience*, *3*(5), 358–362. https://doi.org/10.1038/ngeo830

Bischoff, S. H., & Flesch, L. M. (2018). Normal faulting and viscous buckling in the Tibetan Plateau induced by a weak lower crust. *Nature Communications*, *9*(1), 4952. https://doi.org/10.1038/s41467-018-07312-9

Booker, J. R. (2014). The magnetotelluric phase tensor: A critical review. *Surveys in Geophysics*, *35*(1), 7–40. https://doi.org/10.1007/s10712-013-9234-2

Brown, M. (2001). Crustal melting and granite magmatism: Key issues. *Physics and Chemistry of the Earth, Part A: Solid Earth and Geodesy*, *26*(4–5), 201–212. https://doi.org/10.1016/S1464-1895(01)00047-3

Bürgmann, R., & Dresen, G. (2008). Rheology of the lower crust and upper mantle: Evidence from rock mechanics, geodesy, and field observations. *Annual Review of Earth and Planetary Sciences*, *36*(1), 531–567. https://doi.org/10.1146/annurev.earth.36.031207.124326

Caldwell, T. G., Bibby, H. M., & Brown, C. (2004). The magnetotelluric phase tensor. *Geophysical Journal International*, *158*(2), 457–469. https://doi.org/10.1111/j.1365-246X.2004.02281.x

Chave, A. D., & Jones, A. G. (Eds.). (2012). *The magnetotelluric method: Theory and practice* Cambridge, England: Cambridge University Press. Retrieved from https://doi.org/10.1017/CBO9781139020138

Chen, J., Gaillard, F., Villaros, A., Yang, X., Laumonier, M., Jolivet, L., et al. (2018). Melting conditions in the modern Tibetan crust since the Miocene. *Nature Communications*, *9*(1), 3515–3513. https://doi.org/10.1038/s41467-018-05934-7

Chen, L., Booker, J. R., Jones, A. G., Wu, N., Unsworth, M. J., Wei, W., & Tan, H. (1996). Electrically conductive crust in southern Tibet from INDEPTH magnetotelluric surveying. *Science*, *274*(5293), 1694–1696. https://doi.org/10.1126/science.274.5293.1694

Chen, L., Capitanio, F. A., Liu, L., & Gerya, T. V. (2017). Crustal rheology controls on the Tibetan plateau formation during India-Asia convergence. *Nature Communications*, *8*(1), 1, 15992–8. https://doi.org/10.1038/ncomms15992

Comeau, M. J., Käufl, J. S., Becken, M., Kuvshinov, A. V., Grayver, A. V., Kamm, J., et al. (2018). Evidence for fluid and melt generation in response to an asthenospheric upwelling beneath the Hangai Dome, Mongolia. *Earth and Planetary Science Letters*, *487*, 201–209. https://doi.org/10.1016/j.epsl.2018.02.007

Comeau, M. J., Unsworth, M. J., & Cordell, D. (2016). New constraints on the magma distribution and composition beneath Volcán Uturuncu and the southern Bolivian Altiplano from magnetotelluric data. *Geosphere*, *12*(5), 1391–1421. https://doi.org/10.1130/GES01277.1

Copley, A. (2012). The formation of mountain range curvature by gravitational spreading. *Earth and Planetary Science Letters*, *351-352*, 208–214. https://doi.org/10.1016/j.epsl.2012.07.036

DeVries, P. M. R., & Meade, B. J. (2013). Earthquake cycle deformation in the Tibetan plateau with a weak mid-crustal layer. *Journal of Geophysical Research: Solid Earth*, *118*, 3101–3111. https://doi.org/10.1002/jgrb.50209

Dong, H., & Egbert, G. D. (2019). Divergence-free solutions to electromagnetic forward and adjoint problems: A regularization approach. *Geophysical Journal International*, *216*(2), 906–918. https://doi.org/10.1093/gji/ggy462

Dong, H., Wei, W., Jin, S., Ye, G., Zhang, L., Jing, J., et al. (2016). Extensional extrusion: Insights into south-eastward expansion of Tibetan Plateau from magnetotelluric array data. *Earth and Planetary Science Letters*, *454*, 78–85. https://doi.org/10.1016/j.epsl.2016.07.043

Dong, S., Li, T., Lü, Q. T., Gao, R., Yang, J. S., Chen, X. H., et al. (2013). Progress in deep lithospheric exploration of the continental China: A review of the SinoProbe. *Tectonophysics*, *606*, 1–13. https://doi.org/10.1016/j.tecto.2013.05.038

Duan, X. (2014). A general model for predicting the solubility behavior of H_2O–CO_2 fluids in silicate melts over a wide range of pressure, temperature and compositions. *Geochimica et Cosmochimica Acta*, *125*, 582–609. https://doi.org/10.1016/j.gca.2013.10.018

Egbert, G. D., & Booker, J. R. (1986). Robust estimation of geomagnetic transfer functions. *Geophysical Journal International*, *87*(1), 173–194. https://doi.org/10.1111/j.1365-246X.1986.tb04552.x

Evans, R. L., Hirth, G., Baba, K., Forsyth, D., Chave, A. D., & Mackie, R. L. (2005). Geophysical evidence from the MELT area for compositional controls on oceanic plates. *Nature*, *437*(7056), 249–252. https://doi.org/10.1038/nature04014

Gamble, T. D., Goubau, W. M., & Clarke, J. (1979). Magnetotelluric with a remote magnetic reference. *Geophysics*, *44*(1), 53–68. https://doi.org/10.1190/1.1440923

Gan, W., Zhang, P., Shen, Z.-K., Niu, Z., Wang, M., Wan, Y., et al. (2007). Present-day crustal motion within the Tibetan Plateau inferred from GPS measurements. *Journal of Geophysical Research*, *112*, B08416. https://doi.org/10.1029/2005JB004120

Glover, P. W. J., Hole, M. J., & Pous, J. (2000). A modified Archie's law for two conducting phases. *Earth and Planetary Science Letters*, *180*(3–4), 369–383. https://doi.org/10.1016/S0012-821X(00)00168-0

Gregori, G. P., & Lanzerotti, L. J. (1980). Geomagnetic depth sounding by induction arrow representation: A review. *Reviews of Geophysics*, *18*(1), 203–209. https://doi.org/10.1029/RG018i001p00203

Guo, H., & Keppler, H. (2019). Electrical conductivity of NaCl-bearing aqueous fluids to 900 °C and 5 GPa. *Journal of Geophysical Research: Solid Earth*, *124*, 1397–1411. https://doi.org/10.1029/2018JB016658

Guo, X., Zhang, L., & Su, X. (2018). Melting inside the Tibetan crust? Constraint from electrical conductivity of peraluminous granitic melt. *Geophysical Research Letters*, *45*, 3906–3913. https://doi.org/10.1029/2018GL077804

Haines, S. S., Klemperer, S. L., Brown, L. D., Jingru, G., Mechie, J., Meissner, R., R., et al. (2003). INDEPTH III seismic data: From surface observations to deep crustal processes in Tibet. *Tectonics*, *22*(1), 1–18. https://doi.org/10.1029/2001TC001305

Hashim, L., Gaillard, F., Champallier, R., Le Breton, N., Arbaret, L., & Scaillet, B. (2013). Experimental assessment of the relationships between electrical resistivity, crustal melting and strain localization beneath the Himalayan-Tibetan Belt. *Earth and Planetary Science Letters*, *373*, 20–30. https://doi.org/10.1016/j.epsl.2013.04.026

Hashin, Z., & Shtrikman, S. (1963). A variational approach to the elastic behavior of multiphase minerals: Journal of the mechanics and physics of solids. *Journal of the Mechanics and Physics of Solids*, *11*(2), 127–140. https://doi.org/10.1016/0022-5096(63)90060-7

Huang, F., Xu, J.-F., Chen, J.-L., Wu, J.-B., Zeng, Y.-C., Xiong, Q.-W., et al. (2016). Two Cenozoic tectonic events of N-S and E-W extension in the Lhasa Terrane: Evidence from geology and geochronology. *Lithos*, *245*, 118–132. https://doi.org/10.1016/j.lithos.2015.08.014

Jamieson, R. A., Beaumont, C., Medvedev, S., & Nguyen, M. H. (2004). Crustal channel flows: 2. Numerical models with implications for metamorphism in the Himalayan-Tibetan orogen. *Journal of Geophysical Research*, *109*, B06407. https://doi.org/10.1029/2003JB002811

Jiménez-Munt, I., Fernàndez, M., Vergés, J., & Platt, J. P. (2008). Lithosphere structure underneath the Tibetan Plateau inferred from elevation, gravity and geoid anomalies. *Earth and Planetary Science Letters*, *267*(1–2), 276–289. https://doi.org/10.1016/j.epsl.2007.11.045

Jones, A. G. (1988). Static shift of magnetotelluric data and its removal in a sedimentary basin environment. *Geophysics*, *53*(7), 967–978. https://doi.org/10.1190/1.1442533

Jones, A. G. (1992). Electrical conductivity of the continental lower crust. In D. M. Fountain, R. J. Arculus, & R. W. Kay (Eds.), *Continental lower crust* (pp. 81–143). Amsterdams, Netherlands: Elsevier B.V.

Jones, A. G. (2011). Three-dimensional galvanic distortion of three-dimensional regional conductivity structures: Comment on "Three-dimensional joint inversion for magnetotelluric resistivity and static shift distributions in complex media" by Yutaka Sasaki and max a. Meju. *Journal of Geophysical Research*, *116*, B12104. https://doi.org/10.1029/2011JB008665

Jones, A. G. (2012). Chapter 6. Distortion of magnetotelluric data: Its identification and removal. In A. D. Chave, & A. G. Jones (Eds.), *The Magnetotelluric Method: Theory and Practice* (pp. 219–302). Cambridge, England: Cambridge University Press. https://doi.org/10.1017/CBO9781139020138.008

Jones, A. G. (2016). Proton conduction and hydrogen diffusion in olivine: An attempt to reconcile laboratory and field observations and implications for the role of grain boundary diffusion in enhancing conductivity. *Physics and Chemistry of Minerals*, *43*(4), 237–265. https://doi.org/10.1007/s00269-015-0790-5

Jones, A. G., & Jödicke, H. (1984). Magnetotelluric transfer function estimation improvement by a coherence-based rejection technique. In *SEG Technical Program Expanded Abstracts 1984* (pp. 51–55). Atlanta, United States: Society of Exploration Geophysicists. https://doi.org/10.1190/1.1894081

Kapp, P., Taylor, M. H., Stockli, D., & Ding, L. (2008). Development of active low-angle normal fault systems during orogenic collapse: Insight from Tibet. *Geology*, *36*(1), 7. https://doi.org/10.1130/G24054A.1

Käufl, J. S., Grayver, A. V., Comeau, M. J., Kuvshinov, A. V., Becken, M., Kamm, J., et al. (2020). Magnetotelluric multiscale 3-D inversion reveals crustal and upper mantle structure beneath the Hangai and Gobi-Altai region in Mongolia. *Geophysical Journal International*, *221*(2), 1002–1028. https://doi.org/10.1093/gji/ggaa039

Kelbert, A., Meqbel, N. M., Egbert, G. D., & Tandon, K. (2014). ModEM: A modular system for inversion of electromagnetic geophysical data. *Computers & Geosciences*, *66*, 40–53. https://doi.org/10.1016/j.cageo.2014.01.010

Klemperer, S. L. (2006). Crustal flow in Tibet: Geophysical evidence for the physical state of Tibetan lithosphere, and inferred patterns of active flow. In R. D. Law, M. P. Searle, & L. Godin (Eds.), *Channel Flow, Ductile Extrusion and Exhumation in Continental Collision Zones* (Vol. 268, pp. 39–70). London: Geological Society. https://doi.org/10.1144/GSL.SP.2006.268.01.03, 1

Kukkonen, I. T., Kuusisto, M., Lehtonen, M., & Peltonen, P. (2008). Tectonophysics delamination of eclogitized lower crust: Control on the crust–mantle boundary in the central Fennoscandian shield. *Tectonophysics*, *457*(3-4), 111–127. https://doi.org/10.1016/j.tecto.2008.04.029

Laumonier, M., Gaillard, F., Muir, D., Blundy, J., & Unsworth, M. (2017). Giant magmatic water reservoirs at mid-crustal depth inferred from electrical conductivity and the growth of the continental crust. *Earth and Planetary Science Letters*, *457*, 173–180. https://doi.org/10.1016/j.epsl.2016.10.023

Laumonier, M., Gaillard, F., & Sifre, D. (2014). The effect of pressure and water concentration on the electrical conductivity of dacitic melts: Implication for magnetotelluric imaging in subduction areas. *Chemical Geology*, *418*, 66–76. https://doi.org/10.1016/j.chemgeo.2014.09.019

Le Pape, F., Jones, A. G., Unsworth, M. J., Vozar, J., Wei, W., Jin, S., et al. (2015). Constraints on the evolution of crustal flow beneath Northern Tibet. *Geochemistry, Geophysics, Geosystems*, *16*, 4237–4260. https://doi.org/10.1002/2015GC005828

Le Pape, F., Jones, A. G., Vozar, J., & Wei, W. (2012). Penetration of crustal melt beyond the Kunlun Fault into northern Tibet. *Nature Geoscience*, *5*(5), 330–335. https://doi.org/10.1038/ngeo1449

Ledo, J. (2005). 2-D versus 3-D magnetotelluric data interpretation. *Surveys in Geophysics*, *26*(5), 511–543. https://doi.org/10.1007/s10712-005-1757-8

Lee, J., Hager, C., Wallis, S. R., Stockli, D. F., Whitehouse, M. J., Aoya, M., & Wang, Y. (2011). Middle to late Miocene extremely rapid exhumation and thermal reequilibration in the Kung Co rift, southern Tibet. *Tectonics*, *30*(2), 1–26. https://doi.org/10.1029/2010TC002745

Li, D., & Yin, A. (2008). Orogen-parallel, active left-slip faults in the Eastern Himalaya: Implications for the growth mechanism of the Himalayan Arc. *Earth and Planetary Science Letters*, *274*(1–2), 258–267. https://doi.org/10.1016/j.epsl.2008.07.043

Li, J., & Song, X. (2018). Tearing of Indian mantle lithosphere from high-resolution seismic images and its implications for lithosphere coupling in southern Tibet. *Proceedings of the National Academy of Sciences of the United States of America*, *115*(33), 8296–8300. https://doi.org/10.1073/pnas.1717258115

Li, S., Unsworth, M. J., & Booker, J. R. (2003). Partial melt or aqueous fluid in the mid-crust of Southern Tibet? Constraints from INDEPTH magnetotelluric data. *Geophysical Journal International*, *153*(2), 289–304. Retrieved from. https://doi.org/10.1046/j.1365-246X.2003.01850.x/full

Liu, C., Wu, F., Chung, S., & Zhao, Z. (2011). Fragments of hot and metasomatized mantle lithosphere in Middle Miocene ultrapotassic lavas, southern Tibet. *Geology*, *39*(10), 923–926. https://doi.org/10.1130/G32172.1

Liu, L., & Hasterok, D. (2016). High-resolution lithosphere viscosity and dynamics revealed by magnetotelluric imaging. *Science*, *353*(6307), 1515–1519. https://doi.org/10.1126/science.aaf6542

Lu, Z., Gao, R., Li, H., Li, W., & Xiong, X. (2015). Variation of Moho depth across Bangong-Nujiang Suture in Central Tibet—Results from deep seismic reflection data. *International Journal of Geosciences*, *06*(08), 821–830. https://doi.org/10.4236/ijg.2015.68066

Makovsky, Y., & Klemperer, S. L. (1999). Measuring the seismic properties of Tibetan bright spots: Evidence for free aqueous fluids in the Tibetan middle crust. *Journal of Geophysical Research*, *104*(B5), 10795–10825. https://doi.org/10.1029/1998JB900074

McCaffrey, R., & Nabelek, J. (1998). Role of oblique convergence in the active deformation of the Himalayas and southern Tibet plateau. *Geology*, *26*(8), 691. https://doi.org/10.1130/0091-7613(1998)026<0691:ROOCIT>2.3.CO;2

Mechie, J., Sobolev, S. V., Ratschbacher, L., Babeyko, A. Y., Bock, G., Jones, A. G., et al. (2004). Precise temperature estimation in the Tibetan crust from seismic detection of the α-β quartz transition. *Geology*, *32*(7), 601–604. https://doi.org/10.1130/G20367.1

Murphy, B. S., Liu, L., & Egbert, G. D. (2019). Insights into intraplate stresses and geomorphology in the southeastern United States. *Geophysical Research Letters*, *46*, 8711–8720. https://doi.org/10.1029/2019GL083755

Nabelek, J. (2009). Underplating in the Himalaya-Tibet collision zone revealed by the hi-CLIMB experiment. *Science*, *325*(11), 1371–1374.

Nabelek, P., & Nabelek, J. (2014). Thermal characteristics of the Main Himalaya Thrust and the Indian lower crust with implications for crustal rheology and partial melting in the Himalaya orogen. *Earth and Planetary Science Letters*, *395*, 116–123. https://doi.org/10.1016/j.epsl.2014.03.026

Nelson, K. D., Zhao, W., Brown, L. D., Kuo, J., Che, J., Liu, X., et al. (1996). Partially molten middle crust beneath southern Tibet: Synthesis of project INDEPTH results. *Science*, *274*(5293), 1684–1688. https://doi.org/10.1126/science.274.5293.1684

Nesbritt, B. E. (1993). Electrical resistivities of crustal fluids. *Journal of Geophysical Research*, *98*(B3), 4301–4310. https://doi.org/10.1029/92JB02576

Nomade, S., Renne, P. R., Mo, X., Zhao, Z., & Zhou, S. (2004). Miocene volcanism in the Lhasa block, Tibet: Spatial trends and geodynamic implications. *Earth and Planetary Science Letters*, *221*(1–4), 227–243. https://doi.org/10.1016/S0012-821X(04)00072-X

Pang, Y., Zhang, H., Gerya, T. V., Liao, J., Cheng, H., & Shi, Y. (2018). The mechanism and dynamics of N-S rifting in southern Tibet: Insight from 3-D thermomechanical modeling. *Journal of Geophysical Research: Solid Earth*, *123*, 859–877. https://doi.org/10.1002/2017JB014011

Parkinson, W. D. (1959). Directions of rapid geomagnetic fluctuations. *Geophysical Journal of the Royal Astronomical Society*, *2*(1), 1–14. https://doi.org/10.1111/j.1365-246X.1959.tb05776.x

Parkinson, W. D. (1962). The influence of continents and oceans on geomagnetic variations. *Geophysical Journal of the Royal Astronomical Society*, *6*(4), 441–449. https://doi.org/10.1111/j.1365-246X.1962.tb02992.x

Patino Douce, A. E., & Harris, N. (1998). Experimental constraints on Himalayan Anatexis. *Journal of Petrology*, *39*(4), 689–710. https://doi.org/10.1093/petroj/39.4.689

Pek, J., Santos, F. A. M., & Li, Y. (2011). *Non-linear conjugate gradient magnetotelluric inversion for 2-D anisotropic conductivities* (Vol. 24, pp. 187–206). Neustadt and der Weinstrasse, Germany: Schmucker-Weidelt-Colloquium für Elektromagnetische Tiefenforschung (EMTF).

Pek, J., & Verner, T. (1997). Finite-difference modelling of magnetotelluric fields in two-dimensional anisotropic media. *Geophysical Journal International*, *128*(3), 505–521. https://doi.org/10.1111/j.1365-246X.1997.tb05314.x

Pommier, A. (2013). Interpretation of magnetotelluric results using laboratory measurements. *Surveys in Geophysics*, *35*(1), 41–84. https://doi.org/10.1007/s10712-013-9226-2

Pommier, A., Evans, R. L., Key, K., & Tyburczy, J. A. (2013). Prediction of silicate melt viscosity from electrical conductivity: A model and its geophysical implications Anne. *Geochemistry, Geophysics, Geosystems*, *14*, 1685–1692. https://doi.org/10.1002/ggge.20103

Prouteau, G., Scaillet, B., Pichavant, M., & Maury, R. C. (1999). Fluid-present melting of ocean crust in subduction zones. *Geology*, *27*(12), 1111–1114. https://doi.org/10.1130/0091-7613(1999)027<1111

Renner, J., Evans, B., & Hirth, G. (2000). On the rheologically critical melt fraction. *Earth and Planetary Science Letters*, *181*(4), 585–594. https://doi.org/10.1016/S0012-821X(00)00222-3

Rippe, D., & Unsworth, M. J. (2010). Quantifying crustal flow in Tibet with magnetotelluric data. *Physics of the Earth and Planetary Interiors*, *179*(3–4), 107–121. https://doi.org/10.1016/j.pepi.2010.01.009

Rosenberg, C. L., & Handy, M. R. (2005). Experimental deformation of partially melted granite revisited: Implications for the continental crust. *Journal of Metamorphic Geology*, *23*(1), 19–28. https://doi.org/10.1111/j.1525-1314.2005.00555.x

Royden, L., Burchfiel, B. C., King, R., & Wang, E. (1997). Surface deformation and lower crustal flow in eastern Tibet. *Science*, *276*(5313), 788–790. Retrieved from. http://www.sciencemag.org/content/276/5313/788.short, https://doi.org/10.1126/science.276.5313.788

Sakuma, H., & Ichiki, M. (2016). Electrical conductivity of NaCl-H_2O fluid in the crust. *Journal of Geophysical Research: Solid Earth*, *121*, 577–594. https://doi.org/10.1002/2015JB012219.Received

Schilling, F. R., & Partzsch, G. M. (2001). Quantifying partial melt fraction in the crust beneath and Central Andes and the Tibetan Plateau. *Physics and Chemistry of the Earth, Part A: Solid Earth and Geodesy*, *26*(4-5), 239–246. https://doi.org/10.1016/S1464-1895(01)00051-5

Shinevar, W. J., Behn, M. D., & Hirth, G. (2015). Compositional dependence of lower crustal viscosity. *Geophysical Research Letters*, *42*, 8333–8340. https://doi.org/10.1002/2015GL065459

Simpson, R. W. (1997). Quantifying Anderson's fault types. *Journal of Geophysical Research*, *102*(B8), 17909–17919. https://doi.org/10.1029/97JB01274

Sinmyo, R., & Keppler, H. (2017). Electrical conductivity of NaCl-bearing aqueous fluids to 600 °C and 1 GPa. *Contributions to Mineralogy and Petrology.*, *172*(1), 4. https://doi.org/10.1007/s00410-016-1323-z

Solon, K. D., Jones, A. G., Nelson, K. D., Unsworth, M. J., Kidd, W. F., Wei, W., Tan, H., et al. (2005). Structure of the crust in the vicinity of the Banggong-Nujiang suture in central Tibet from INDEPTH magnetotelluric data. *Journal of Geophysical Research*, *110*, B10102. https://doi.org/10.1029/2003JB002405

Styron, R. H., Taylor, M. H., & Murphy, M. A. (2011). Oblique convergence, arc-parallel extension, and the role of strike-slip faulting in the High Himalaya. *Geosphere*, *7*(2), 582–596. https://doi.org/10.1130/GES00606.1

Styron, R. H., Taylor, M. H., & Sundell, K. (2015). Accelerated extension of Tibet linked to the northward underthrusting of Indian crust. *Nature Geoscience*, *8*(2), 131–134. https://doi.org/10.1038/ngeo2336

Tao, W., & Shen, Z. (2008). Heat flow distribution in Chinese continent and its adjacent areas. *Progress in Natural Science*, *18*(7), 843–849. https://doi.org/10.1016/j.pnsc.2008.01.018

Tapponnier, P., Peltzer, G., Le Dain, A. Y., Armijo, R., & Cobbold, P. R. (1982). Propagation extrusion tectonics in Asia: New insights from experiments with plasticine. *Geology*, *10*(December), 611–616. https://doi.org/10.1130/0091-7613(1982)10<611:PETIAN>2.0.CO;2

Taylor, M. H., & Yin, A. (2009). Active structures of the Himalayan-Tibetan orogen and their relationships to earthquake distribution, contemporary strain field, and Cenozoic volcanism. *Geosphere*, *5*(3), 199–214. https://doi.org/10.1130/GES00217.1

ten Grotenhuis, S. M., Drury, M. R., Spiers, C. J., & Peach, C. J. (2005). Melt distribution in olivine rocks based on electrical conductivity measurements. *Journal of Geophysical Research*, *110*, B12201. https://doi.org/10.1029/2004JB003462

Thompson, A. B., & Connolly, J. A. D. (1995). Melting of the continental crust: Some thermal and petrological constraints on anatexis in continental collision zones and other tectonic settings. *Journal of Geophysical Research*, *100*(B8), 15565–15579. https://doi.org/10.1029/95JB00191

Tozer, D. C. (1981). The mechanical and electrical properties of Earth's asthenosphere. *Physics of the Earth and Planetary Interiors*, *25*(3), 280–296. https://doi.org/10.1016/0031-9201(81)90072-8

Unsworth, M. J., Jones, A. G., Wei, W., Marquis, G., Gokarn, S. G., Spratt, J. E., & the INDEPTH-MT team (2005). Crustal rheology of the Himalaya and Southern Tibet inferred from magnetotelluric data. *Nature*, *438*(7064), 78–81. https://doi.org/10.1038/nature04154

Unsworth, M. J., Wei, W., Jones, A. G., Li, S., Bedrosian, P. A., Booker, J. R., et al. (2004). Crustal and upper mantle structure of northern Tibet imaged with magnetotelluric data. *Journal of Geophysical Research*, *109*, B02403. https://doi.org/10.1029/2002JB002305

Waff, H. S. (1974). Theoretical considerations of electrical conductivity in a partially molten mantle and implications for geothermometry. *Journal of Geophysical Research*, *79*(26), 4003–4010. https://doi.org/10.1029/JB079i026p04003

Wang, C., Dai, J., Zhao, X., Li, Y., Graham, S. A., He, D., et al. (2014). Outward-growth of the Tibetan Plateau during the Cenozoic: A review. *Tectonophysics*, *621*, 1–43. https://doi.org/10.1016/j.tecto.2014.01.036

Wang, C., Chen, W., & Wang, L. (2013). Temperature beneath Tibet. *Earth and Planetary Science Letters*, *375*(August), 326–337. https://doi.org/10.1016/j.epsl.2013.05.052

Wang, Q., Hawkesworth, C. J., Wyman, D., Chung, S., Wu, F., Li, X., et al. (2016). Pliocene-Quaternary crustal melting in central and northern Tibet and insights into crustal flow. *Nature Communications*, *7*(1), 1, 11888–11. https://doi.org/10.1038/ncomms11888

Wang, R., Richards, J. P., Hou, Z., Yang, Z., & Dufrane, S. A. (2014). Increased magmatic water content - The key to Oligo-Miocene porphyry Cu-Mo ± Au formation in the eastern Gangdese Belt, Tibet. *Economic Geology*, *109*(5), 1315–1339. https://doi.org/10.2113/econgeo.109.5.1315

Wannamaker, P. E. (1986). Electrical conductivity of water-undersaturated crustal melting. *Journal of Geophysical Research*, *91*(B6), 6321. https://doi.org/10.1029/JB091iB06p06321

Wei, W., Unsworth, M. J., Jones, A. G., Booker, J. R., Tan, H., Nelson, K. D., et al. (2001). Detection of widespread fluids in the Tibetan crust by magnetotelluric studies. *Science*, *292*(April), 1999–2001.

Weidelt, P. (1985). Construction of conductance bounds from magnetotelluric impedances. *Journal of Geophysics - Zeitschrift Fur Geophysik*, *57*(3), 191–206.

Weinberg, R. F., & Hasalová, P. (2015). Water-fluxed melting of the continental crust: A review. *Lithos*, *212-215*, 158–188. https://doi.org/10.1016/j.lithos.2014.08.021

Xie, C., Jin, S., Wei, W., Ye, G., Zhang, L., Dong, H., & Yin, Y. (2017). Varying Indian crustal front in the southern Tibetan Plateau as revealed by magnetotelluric data. *Earth, Planets and Space*, *69*(1), 147. https://doi.org/10.1186/s40623-017-0734-z

Yin, A., & Taylor, M. H. (2011). Mechanics of V-shaped conjugate strike-slip faults and the corresponding continuum mode of continental deformation. *Bulletin of the Geological Society of America*, *123*(9–10), 1798–1821. https://doi.org/10.1130/B30159.1

Zhou, B., Liang, X., Lin, G., Tian, X., Zhu, G., Mechie, J., & Teng, J. (2019). Upper crustal weak zone in Central Tibet: An implication from three-dimensional seismic velocity and attenuation tomography results. *Journal of Geophysical Research: Solid Earth*, *124*, 4654–4672. https://doi.org/10.1029/2018JB016653

Zhu, D., Li, S., Cawood, P. A., Wang, Q., Zhao, Z., Liu, S., & Wang, L. (2016). Lithos assembly of the Lhasa and Qiangtang terranes in central Tibet by divergent double subduction. *Lithos*, *245*(06), 7–17. https://doi.org/10.1016/j.lithos.2015.06.023